19e Journées de l'Hydrodynamique
26 – 28 novembre 2024, Nantes

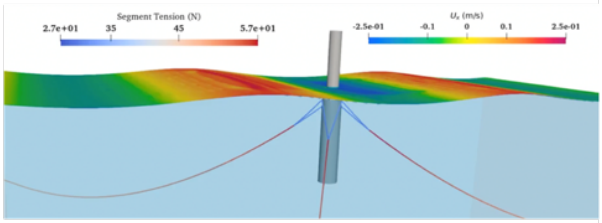

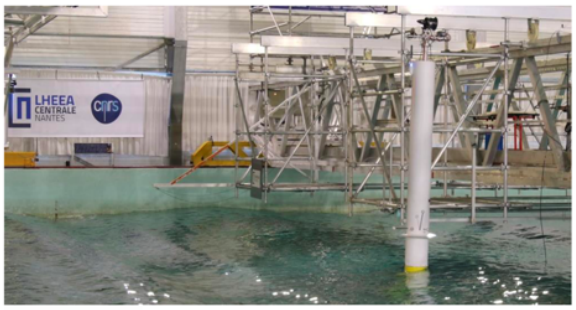

EXPERIMENTAL AND NUMERICAL INVESTIGATIONS OF WAVE LOADS ON A FIXED BOX BARGE WITH A MOONPOOL AND DAMPING PLATES IN A TWO-DIMENSIONAL WAVE FLUME

S.-Y. HAN[(1)], B.BOUSCASSE[(1)], R. MARIANI[(2)], A. COURBOIS[(2)], D. LE TOUZÉ[(1)], and L. KIMMOUN[(3)]

seung-yoon.han@ec-nantes.fr; benjamin.bouscasse@ec-nantes.fr; riccardo.mariani@bw-ideol.com adrien.courbois@bw-ideol.com; david.letouze@ec-nantes.fr

[(1)]Nantes Université, École Centrale Nantes, CNRS, LHEEA, UMR 6598, F-44000 Nantes, France
[(2)]BW-Ideol, 147 avenue du Jujubier, 13600, La Ciotat, France
[(3)]Aix-Marseille Université, CNRS, Centrale Marseille, IRPHE, UMR 7342, Marseille, France

Summary

The study aims to investigate wave loads on a box barge with a moonpool and damping plates in a two-dimensional problem using experimental, numerical, and theoretical methods. An experiment was conducted in a two-dimensional wave flume at Ecole Centrale Marseille (ECM). The experimental model, composed of two pontoons, each equipped with a horizontal skirt (damping plate) in correspondence with its bottom, was fixed at the tank. Two configurations, with and without skirts, were tested in regular waves with various wave steepness and wave periods. A load cell was installed on the model to measure wave loads. Resistive wave gauges were used to measure free-surface elevations around the model by focusing on the incident, reflected, and transmitted waves. Dedicated numerical analysis was performed for one wave steepness using a Navier-Stokes solver (CFD) based on Openfoam. A theoretical model based on the potential flow theory was developed to compute the linear wave elevation and wave excitation forces using eigenfunction expansion method on decomposed domains, including the dissipation effect. The CFD and theoretical models are generally able to predict the wave excitation forces. Furthermore, by introducing dissipation into the moonpool, the theoretical model was able to capture the mean drift forces using the far-field method.

I – Introduction

Floating offshore wind turbines are a cost-effective way to harvest wind energy, but the platform faces challenges in withstanding harsh wave environments. To address this challenge, various types of floaters have been studied. Some concepts have progressed from a single prototype to larger-scale implementations for floating wind farms.

One notable type of floater is a box barge-type floater with a moonpool [1]. The moonpool reduces the water plane area of the barge, which optimizes the stability and performance of the floating system. Choisnet (2015) [2] described how the moonpool, if opportunely configured, could partially reduce the heave motion induced by the waves through the load generated on the floating structure by the mass of water oscillating inside the moonpool. Additionally, the floater can be equipped with damping plates (skirts), gaining more hydrodynamic added mass and damping of the floating system [3]. As a result, both moonpool and the plates reduce wave-induced motion response to the dominant wave periods, particularly by enhancing energy dissipation for motions of interest.

The moonpool serves various marine and offshore applications, facilitating operations such as drilling risers, dynamic cables, and remotely operated underwater vehicles. However, the free surface inside the moonpool can behave violently at resonance, making it essential to predict and mitigate these effects. Molin (2001) [4] identified two types of resonant behaviors theoretically based on linearized potential flow theory : piston and sloshing modes. The piston mode was further investigated using a two-dimensional barge with a moonpool through forced heave oscillation tests conducted in the wave flume [5]. Wave-induced responses were experimentally studied in regular waves [6], and compared with the two numerical methods that solve the Laplace equation and the Navier-Stokes equations, respectively. Additional structures such as cofferdams or recesses were examined both experimentally and numerically to investigate the reduction of free surface behavior in the moonpool [7, 8].

The potential flow theory is effective in predicting the resonant frequency, but it tends to overestimate the resonant response. Chen (2004) [9] introduced the concept of a fairly perfect fluid, following Guével (1982) [10]. This approach involves adding a linear dissipation term to the momentum equation for an incompressible, inviscid fluid and irrotational flow. It has been validated against experimental results, showing efficiency in predicting free surface elevation by identifying the appropriate level of dissipation from high-fidelity methods, such as experiments and Navier-Stokes equation solvers (CFD). This formulation is implemented in Boundary Element Method (BEM) solvers and is applied to various engineering applications, including gap resonance, moonpools, and sloshing tanks.

Earlier research [11] examined the motion responses of the box barge-type floater with a moonpool and skirts in regular waves using model-scale experiments and CFD methods for both model and full-scale simulations. In Adrien (2018) [12], the full geometry was then simplified into a fixed two-dimensional box-shaped pontoon, both with and without skirts, while excluding the moonpool. This simplification aimed to analyze the effects of the skirts on horizontal mean drift forces and demonstrated that energy dissipation increases due to the presence of the skirt.

The present study extends the previous research [12], by studying the wave loads exerted on a fixed two-dimensional box barge equipped with a moonpool and horizontal skirts fixed in correspondence with its bottom through experimental, numerical, and theoretical methods. Two configurations, one with skirts and one without, are studied in regular waves. The experimental model and setup in a wave flume are first detailed. The numerical model is presented and validated against experimental measurements of free surface elevation. Theoretical formulations, based on the fairly perfect fluid assumption [9, 10], are developed by considering the moonpool and skirts using the domain decomposition method along with eigenfunction expansions. The measured wave excitation forces are compared with the numerical and theoretical calculations, as well as horizontal mean drift forces obtained from the far-field method. Finally, a discussion focuses on the effects of moonpools and skirts on the wave loads.

II – Experiment

An experiment was conducted in a two-dimensional wave flume at Ecole Centrale Marseille (ECM) presented in the sketch of Figure 1, which is 16.7 m in length, 0.65 m in width, and 0.628 m in water depth.

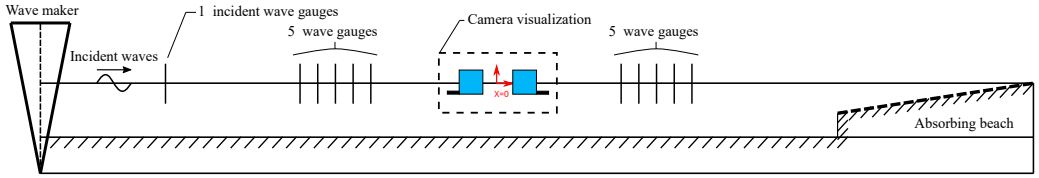

FIGURE 1 – Experimental setup in the two-dimensional wave flum at ECM.

The flume is equipped with a flap wave maker and a wave-absorbing beach to minimize the wave reflection effect. The side wall of the flume is made of glass, which allows a camera to capture free surface deformation and flow field.

The experimental model consisted of two pontoons (blue) and skirts (black), with a moonpool in the middle. The main dimensions are given in Table 1 and presented in the sketch of Figure 3. The reduced scale model could be considered representative of a real wind turbine floating foundation by assuming a scale ratio of around 1/50. The model was designed with a breadth of 0.644 m to prevent contact with the tank wall, taking into account the measurement of wave-induced forces and the use of a freely floating test in the upcoming experimental campaigns. This design resulted in a 3 mm gap on both sides.

Two configurations were considered, with and without skirts, in order to investigate the effects of skirts on the wave excitation forces. Regular waves were tested with various wave steepness (H/λ, with wave height H and wavelength λ) to examine nonlinearity and thirteen wave periods T ranging from 0.55 to 2.5 seconds. In this study, three-wave steepnesses ($H/\lambda = 0.01, 0.02, 0.03$) were selected to verify the numerical and theoretical models.

TABLE 1 – Main dimensions of the model.

Main dimensions		Unit	Value
Length of model	L	m	0.84
Breadth of model	B	m	0.644
Length of pontoon	l_p	m	0.2
Length of damping pool	l_d	m	0.44
Length of skirt	l_s	m	0.06
Thickness of skirt	t_s	m	0.005
Draft	d_1	m	0.14
Depth of skirt	d_2	m	0.135

Thirteen resistive wave gauges were placed in the tank to measure the wave deformation around the model. One wave gauge was positioned near the wave maker to measure the incident wave elevation, and two groups of five wave gauges were placed before and after the model to measure the reflected and transmitted wave elevations. The two remaining gauges were positioned inside the moonpool to monitor the behavior of the free surface on each side of the wall. The model was fixed to a carriage and connected through a 6-axis load cell to measure the wave excitation loads on the model. The data was acquired at a sampling rate of 200 Hz. Furthermore, a video camera with a resolution of 2064x1600 pixels and a frame rate of 100/s was used to capture the flow around the model.

III – Computational Fluid Dynamics

Dedicated numerical simulations were performed using a two-phase incompressible Reynolds Averaged Navier-Stokes Equations (RANSE) solver, *foamStar*. The numerical code has been co-developed by Ecole Centrale Nantes and Bureau Veritas [13, 14] for wave generation and floating body dynamics. It is based on *interDyMFoam* in OpenFOAM, where the volume of fluid (VOF) method is employed for capturing the interface with a volume fraction α, where 0 for air, 1 for water. Practically, the free surface is defined as the isosurface $\alpha = 0.5$.

The governing equations of the mixture fluid written according to the Navier-Stokes equations are presented as follows :

$$\nabla \cdot \mathbf{u} = 0 \tag{1}$$

$$\frac{\partial(\rho\mathbf{u})}{\partial t} + \boldsymbol{\nabla} \cdot (\rho\mathbf{u}\mathbf{u}) = -\boldsymbol{\nabla} p_d - \mathbf{g} \cdot \mathbf{x}\boldsymbol{\nabla}\rho + \boldsymbol{\nabla} \cdot (\mu\boldsymbol{\nabla}\mathbf{u}) + \boldsymbol{\nabla}\mu \cdot (\boldsymbol{\nabla}\mathbf{u})^T \tag{2}$$

$$\frac{\partial\alpha}{\partial t} + \nabla \cdot (\alpha\mathbf{u}) + C_\alpha \nabla \cdot \{\alpha\,(1-\alpha)\,\mathbf{u}_r\} = 0 \tag{3}$$

where $\mathbf{u}$ is the fluid velocity and $\mathbf{u}_r = (\mathbf{u}_{water} - \mathbf{u}_{air})$ is the relative velocity between water and air at the interface. ρ is the fluid density, μ is the dynamic viscosity, $\mathbf{g}$ is the gravitational acceleration. $p_d = p - \rho\mathbf{g}\cdot\mathbf{x}$ is the dynamic pressure and p is the pressure. C_α is an interface compression term, which enables the sharp interface to be kept artificially.

A single wave steepness, $H/\lambda = 0.03$, was studied with seven wave periods (0.8, 0.95, 1.1, 1.25, 1.4, 1.55, 1.8 sec). The free surface $k-\omega$ SST turbulence model was used with the 2nd order Crank-Nicolson (CN, 2nd order) time integral scheme. The total length of the two-dimensional computational domain is 5λ, involving the wave forcing zone [15] in the inlet and damping zone in the outlet, resulting in 2λ of the pure CFD domain. The grids on the free surface, as well as the skirts and corners of the pontoons, were refined as illustrated in Figure 2. The boundary conditions used in this study are listed in Table 2.

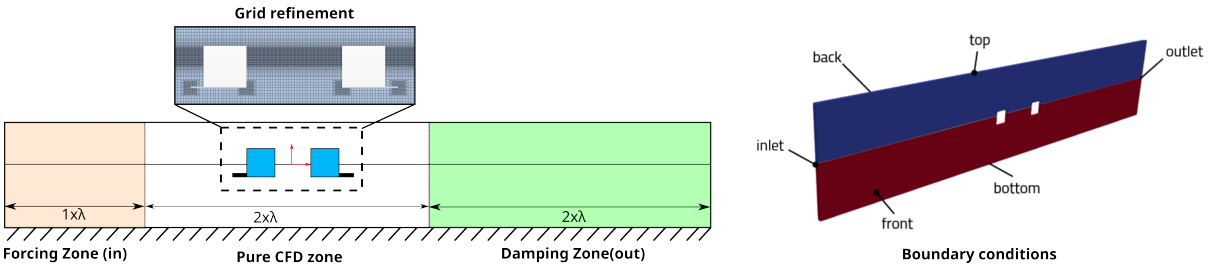

FIGURE 2 – Two-dimensional computational domain and boundary conditions.

TABLE 2 – Boundary conditions for the free surface $k-\omega$ SST turbulence model.

Quantity	inlet/outlet	top	bottom	front/back	body
alpha	waveAlpha	inletOutlet	zeroGradient	empty	zeroGradient
U	waveVelocity	pressureInletOutletVelocity	fixedValue	empty	movingWallVelocity
p_rgh	zeroGradient	totalPressure	zeroGradient	empty	fixedFluxPressure
k	zeroGradient	zeroGradient	zeroGradient	empty	kqRWallFunction
omega	zeroGradient	zeroGradient	zeroGradient	empty	omegaWallFunction
nut	calculated	calculated	calculated	empty	nutUSpaldingWallFunction

IV – Potential flow theory model with dissipations

A linear diffraction potential flow theory model was developed based on a fairly perfect fluid [10] to introduce the dissipation into the moonpool with the assumption of incompressible and inviscid fluid and irrotational flow ($\mathbf{u} = \nabla\phi$). As presented in Guével (1992) [10] and Chen (2011) [9], the fairly perfect fluid can be derived by incorporating the dissipative force, $\mathbf{f} = -\varepsilon\mathbf{u}$, in the momentum equation which enables the treatment of the over-prediction of the free surface trapped in the moonpool. Therefore, the modified Bernoulli equation can be written with the velocity potential [9] :

$$p = -\rho\left(\frac{\partial\phi}{\partial t} + \frac{1}{2}\nabla\phi\cdot\nabla\phi + gz + \varepsilon\phi\right) \tag{4}$$

where ϕ is the velocity potential and ε is the dissipation parameters.

IV – 1 The boundary value problems

Figure 3 describes the two-dimensional problems of a box with a moonpool and skirts, where S_F is the free surface, S_{GF} is the free surface in the gap, S_B is the body surface, S_b is the sea bed and S_∞ is a lateral boundary.

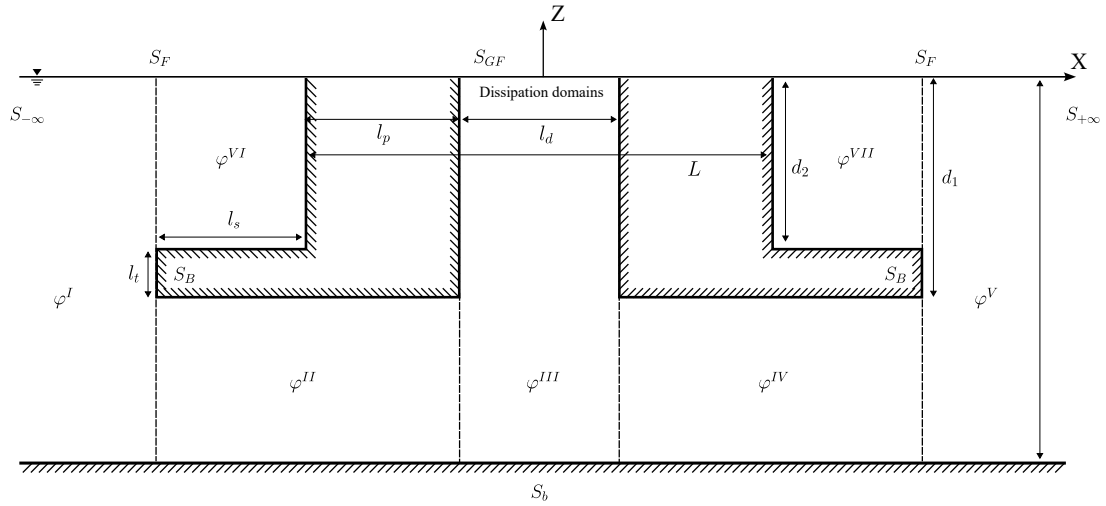

FIGURE 3 – Description of the 2D problem of a box with a moonpool and skirts.

The linearization of the boundary condition is considered by assuming a small wave amplitude. With the time-harmonic assumption with the circular frequency ω, the velocity potential can be expressed as $\phi(X,Z,t) = \mathcal{R}\{\varphi(X,Z)\,e^{-i\omega t}\}$.

Therefore, the boundary value problem of the spatial function φ is :

$$\nabla^2\varphi = 0 \quad \text{in} \quad \Omega \tag{5}$$

$$\frac{\partial\varphi}{\partial z} = \frac{\omega^2}{g}(1+if)\,\varphi \quad \text{on} \quad z = 0 \tag{6}$$

$$\frac{\partial\varphi}{\partial n} = 0 \quad \text{on} \quad S_B \tag{7}$$

$$\frac{\partial\varphi}{\partial z} = 0 \quad \text{on} \quad z = -h \tag{8}$$

where f is a dissipation factor ($f = \varepsilon/\omega$), and Equation 6 represents a combined free surface boundary condition, which is equivalent to the classical one when $f = 0$.

The fluid domain is divided into seven subdomains as presented in Figure 3, considering the moonpool and skirt. Specifically, region III is designated as a dissipation domain to address the non-physically violent free surface responses within the moonpool. It is important to note that the dissipation caused by the skirt is not included in this study.

General solutions of velocity potentials are developed with a series of eigenfunctions on the decomposed fluid domains. The solutions for each domain are summarized in Table 3, along with their corresponding dispersion relations. In particular, in region III, complex eigenvalues arise in the dispersion relation due to the dissipation factor. These complex eigenvalues are obtained using a perturbation method [16].

The general solutions are matched on the interface of subdomains based on the hypothesis of normal velocity and pressure continuity [17], known as matched eigenfunction expansion methods (MEEM). The unknown coefficients in the general solutions denoted A and B, can be determined by solving a linear system after truncating the infinite series to finite, N. In this study, N is set to 20.

TABLE 3 – General solutions of decomposed domains in the two-dimensional problem.

Potential	General solutions	Eigenvalues
$\varphi^I = \varphi_I + \varphi_p$	$-\frac{igA}{\omega} f_0(z) e^{ik_0 x} + A_{10} \cosh k_0(z+h) e^{-ik_0 x} + \sum_{n=1}^{\infty} A_{1n} \cos k_n(z+h) e^{k_n x}$	$\omega^2/g = k_0 \tanh k_0 h = -k_n \tan k_n h$
φ^{II}	$A_{20}x + B_{20} + \sum_{n=1}^{\infty} (A_{2n} e^{\alpha_n x} + B_{3n} e^{-\alpha_n x}) \cos \alpha_n(z+h)$	$\alpha_n = n\pi/(h-d_1)$
φ^{III}	$(A_{30} e^{-i\gamma_0 x} + B_{30} e^{i\gamma_0 x}) \cosh \gamma_0(z+h) + \sum_{n=1}^{\infty} (A_{3n} e^{\gamma_n x} + B_{3n} e^{-\gamma_n x}) \cos \gamma_n(z+h)$	$(1+if)\omega^2/g = \gamma_0 \tanh \gamma_n h = -\gamma_n \tan \gamma_n h$
φ^{IV}	$A_{40}x + B_{40} + \sum_{n=1}^{\infty} (A_{4n} e^{\alpha_n x} + B_{4n} e^{-\alpha_n x}) \cos \alpha_n(z+h)$	$\alpha_n = n\pi/(h-d_1)$
φ^{V}	$A_{50} \cosh k_0(z+h) e^{ik_0 x} + \sum_{n=1}^{\infty} A_{5n} \cos k_n(z+h) e^{k_n x}$	$\omega^2/g = k_0 \tanh k_0 h = -k_n \tan k_n h$
φ^{VI}	$\left(A_{60} e^{-i\beta_0 x} + B_{60} e^{i\beta_0 x}\right) \cosh \beta_0(z+d_2) + \sum_{n=1}^{\infty} \left(A_{6n} e^{\beta_n x} + B_{6n} e^{-\beta_n x}\right) \cos \beta_n(z+d_2)$	$\omega^2/g = \beta_0 \tanh \beta_0 d_2 = -\beta_n \tan \beta_n d_2$
φ^{VII}	$\left(A_{70} e^{-i\beta_0 x} + B_{70} e^{i\beta_0 x}\right) \cosh \beta_0(z+d_2) + \sum_{n=1}^{\infty} \left(A_{7n} e^{\beta_n x} + B_{7n} e^{-\beta_n x}\right) \cos \beta_n(z+d_2)$	$\omega^2/g = \beta_0 \tanh \beta_0 d_2 = -\beta_n \tan \beta_n d_2$

* φ_I is the incident wave potential where $f_0(z) = \cosh k_0(z+h)/\cosh k_0 h$ and φ_p is the perturbed wave potential.

IV – 2 Modified horizontal mean drift forces using far-field method

As described in Maruo and Newman [18, 19], the horizontal forces can be derived using the conservation of momentum equation after time averaging, known as the far-field method. However, because of the presence of the dissipation domain, we have an additional term that appears in the equation for horizontal drift forces :

$$\overline{F}_x = -\overline{\iint_{S_\infty} (p n_x + u_x u_n)\, dS} - \rho \overline{\iint_{S_d} \varepsilon \phi n_x dS} \tag{9}$$

where S_d is the dissipative surface in the moonpool region.

By substituting the velocity potentials of domains I, II, and V, we can get the following expression for the horizontal forces :

$$\overline{F}_x = \frac{1}{2}\rho g \frac{C_g}{C_p} \left(A^2 + A_R A_R^* - A_T A_T^*\right) + \frac{\rho \omega f}{2} \mathcal{X} \tag{10}$$

where $A_R = \frac{i\omega}{g} A_{10} \cosh k_0 h$, $A_T = \frac{i\omega}{g} A_{50} \cosh k_0 h$, and $\mathcal{X} = \varphi^{III} \eta^* \Big|_{x=-b_d/2, z=0} - \varphi^{III} \eta^* \Big|_{x=b_d/2, z=0}$.
The superscript * is for the complex conjugate.

In Equation 10, Maruos's formula, $A^2 = A_R A_R^* + A_T A_T^*$ [18], is not valid, as the modeling of the fairly perfect fluid in the moonpool leads to artificial energy dissipation.

IV – 3 Determination of the dissipation factor

To determine the dissipation factor, f, we analyzed the free surface located in the middle of the moonpool, calculated through CFD and MEEM models, for both configurations, with and without skirts. The linear free surface elevation in the dissipation region is calculated using the following equation :

$$\eta = \frac{\omega}{g}(i - f)\,\varphi^{III} \quad \text{on} \quad z = 0 \tag{11}$$

Figure 4 shows the response amplitude operator (RAO) of the free surface elevation at the center of the moonpool. According to the potential flow theory model, the free surface RAO shows the largest peak at around 1.3 seconds, which aligns with the resonance of the piston mode presented by Molin (2001) [4].

The theoretical model demonstrates good agreement with the CFD results when incorporating the dissipation factor of $f = 0.1$. Additionally, the sharp peak observed around 0.53 seconds, which is close to the frequency of the second sloshing mode, is also dampened. Therefore, in the following results, we will keep the dissipation factor, $f = 0.1$, for the computation of the theoretical model.

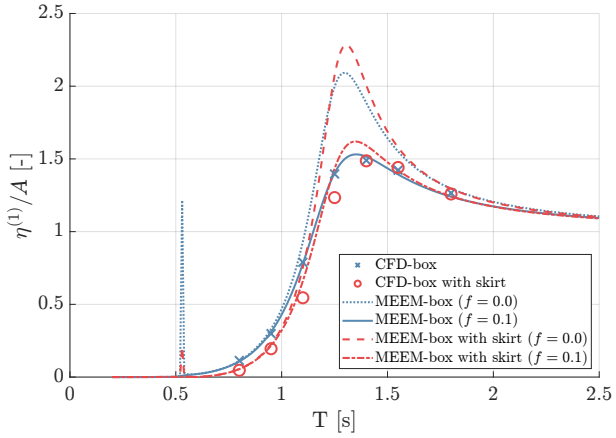

FIGURE 4 – RAO of free surface elevation in the moonpool.

V – Data analysis

The time series (from model tests and CFD simulations) were filtered out by a low-pass filter using a cut-off frequency of 5.0 Hz. This does not really modify the CFD data but it removes the noise from the load cell. A time window is selected for each signal beginning after the transient period with an integer number of wave periods, N, chosen to minimize the wave reflection from the wave-absorbing beach. The Fourier analysis was then used to extract the harmonic content from the time history within the selected window (NT).

This selection process can be quite challenging since the steady-state window becomes notably short for the experiments with large wave periods. In contrast, it is somewhat easier with the CFD, because of the better wave absorption, though the evaluation of the drift forces remains sensitive to the selected time window.

Moreover, the mean drift forces are relatively low compared to the sensor measurement range, and the direct measurement by averaging the force over the time window carries significant uncertainties. To address this, we used a multi-sensor approach to analyze the

waves, enabling us to determine the amplitudes of reflected and transmitted waves by minimizing the quadratic error, as described in Courbois (2018) [12]. These amplitudes were then utilized to evaluate the horizontal mean drift forces based on the two-dimensional far-field method [18, 19, 20],

$$F_d = \frac{1}{2}\rho g \frac{C_g}{C_p}\left(A^2 + A_R A_R^* - A_T A_T^*\right) \tag{12}$$

where $C_g = \frac{\omega}{2k_0}\left(1 + \frac{2k_0 h}{\sinh 2k_0 h}\right)$ and $C_p = \frac{\omega}{k_0}$ are the group and phase velocities. A, A_R and A_T denote the incident, reflected and transmitted wave amplitudes. The formula given in Equation 12 is the same as the one given for the potential flow model in Equation 10, without the dissipation term ($f = 0$).

VI – Results

VI – 1 Validation of the CFD simulations

A snapshot of the CFD simulation is compared with a picture of the experimental test in Figure 5 for the case with $H/\lambda = 0.03$ and $T = 1.55$ s. In the camera, the free surface is visualized by the contrast of light from the floor, while the black solid line represents the free surface in the numerical simulations. The free surface elevation computed with the CFD is similar to the one pictured.

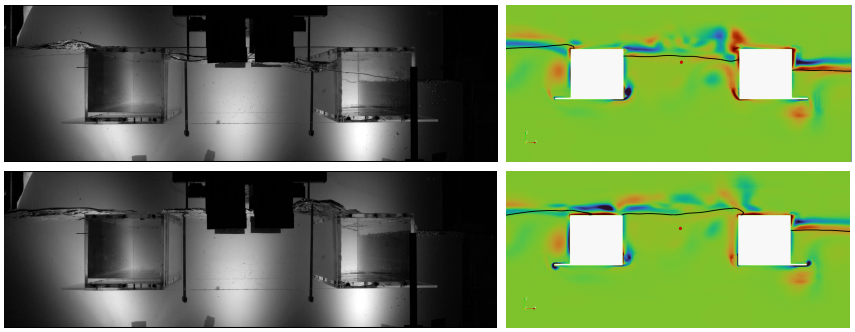

FIGURE 5 – Comparison of free-surface deformations in regular waves with $H/\lambda = 0.03$ and $T = 1.55$ s : experimental (left) and numerical (right) results.

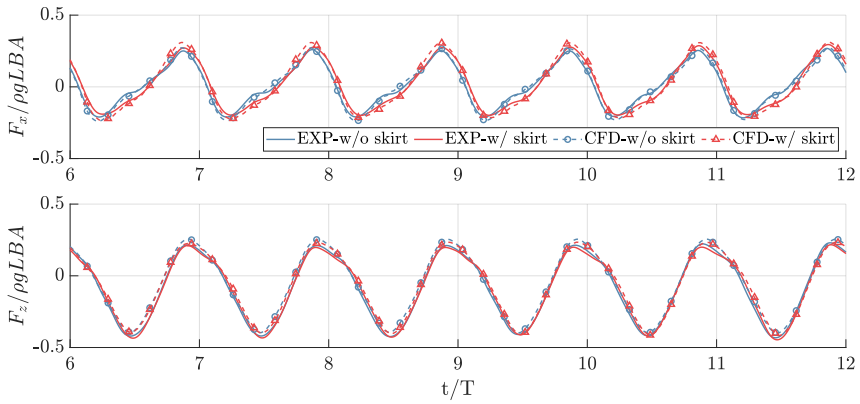

FIGURE 6 – Comparison of wave excitation forces time series in regular waves with $H/\lambda = 0.03$ and $T = 1.55$ s : experimental (solid) and numerical (dashed) results.

The comparison between experimental and CFD wave excitation load time histories is presented in Figure 6 for the same wave condition. Both cases, with and without the skirt, are presented, demonstrating strong agreement between the experimental data and the CFD results. Additionally, there is consistent repeatability over time in the forces time series.

VI – 2 The first harmonic operators

The first harmonic force components measured from the load cell are compared with those obtained from the CFD and the first-order results from the theoretical model (MEEM) as shown in Figures 7 and 8. In the measurements, the horizontal forces show a weak dependence on wave steepness, both with and without skirts. In contrast, the vertical forces exhibit significant variation relative to the steepness in long wave periods. The presence of skirts slightly increases the horizontal forces but diminishes the first peak in vertical forces compared to the model without skirts and shifts this peak to shorter wave periods. Additionally, the vertical forces on the model with skirts increase with wave steepness around a period of $T = 1$ s, where theoretical model gives a minimum value. Around this period for the case with skirts, at the lowest wave steepness, the vertical forces are nearly zero, which aligns with the theoretical model. However, as the steepness increases, the discrepancy from the theoretical predictions becomes apparent. Generally, the CFD and theoretical models with the dissipation well predict the experimental measurements.

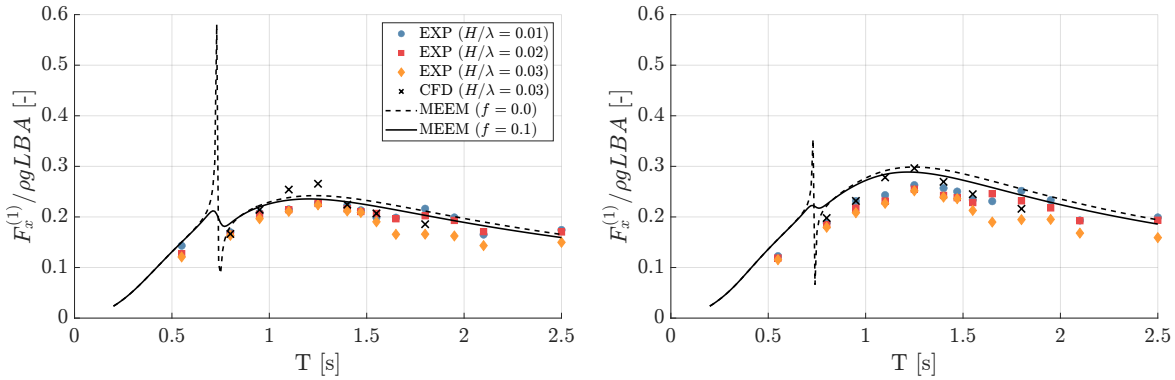

FIGURE 7 – 1^{st} harmonic operator of $F_x^{(1)}$: model without (left) and with skirts (right).

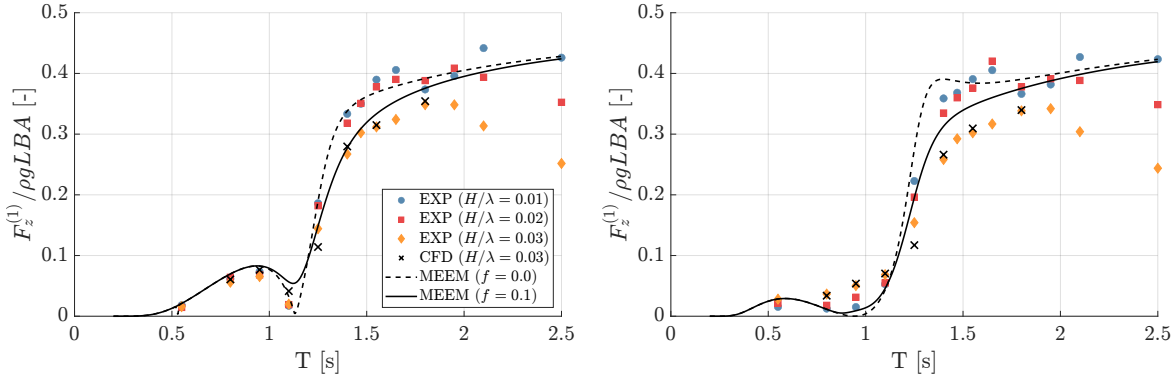

FIGURE 8 – 1^{st} harmonic operator of $F_z^{(1)}$: model without (left) and with skirts (right).

VI – 3 The horizontal mean drift forces

The horizontal drift forces are presented for each wave excitation period in Figure 9. Two series of results are presented for the experimental measurement and the CFD computations : the direct measurement obtained by averaging the horizontal loads (LC for load cell or NF for near-field method) and the far-field (FF) estimation. The comparison focuses on a single steepness of $H/\lambda = 0.03$, as the force values for lower wave steepness result in smaller values that are more challenging to measure.

Generally, the drift forces estimated by the far-field method with CFD and experimental data are very similar. They are also mostly comparable with the MEEM value with the dissipation ($f = 0.1$). However, direct measurement or CFD integration results are larger from the far-field estimation in the long-wave period region. This is particularly true for the case with the skirt, as it may lead to large energy dissipation and consequently possible errors in the far-field estimation. The CFD values obtained for cases T=1.1 s and T= 1.3 s are much larger than the load cell measurements. Uncertainties in the measurements of both the incoming waves and the loads may contribute to this discrepancy, as well as possibly some inaccuracies in the CFD simulations for these conditions characterized by large vortices in the flow.

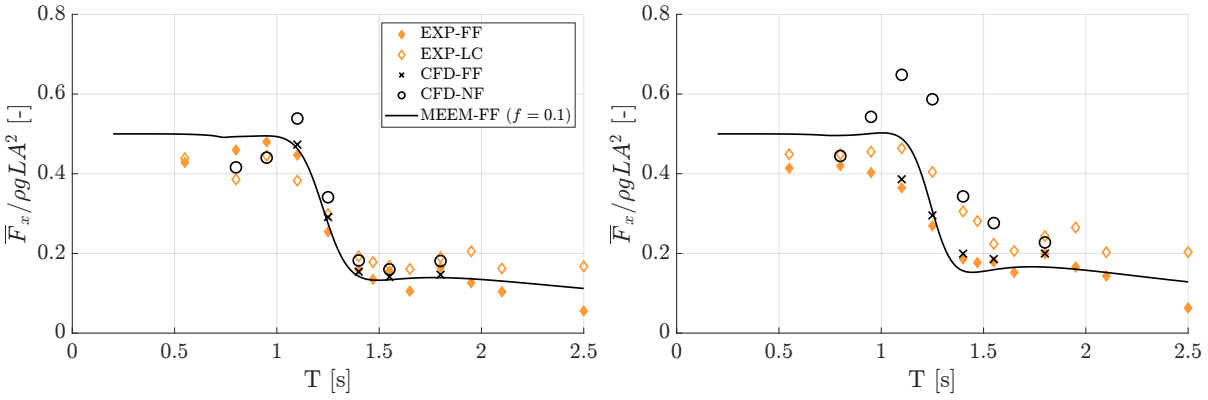

FIGURE 9 – Comparison of the direct measurements (NF or LC) and the far-field (FF) method for horizontal mean drift forces in regular waves with wave steepness $H/\lambda = 0.03$: model without (left) and with skirts (right).

A further comparison is given in Figure 10 for the far-field method with various wave steepnesses. The drift forces differ depending on the presence of skirts and vary with wave steepness, except for the skirtless model in the short wave period region. Overall, the mean drift forces are slightly larger for the model with skirts compared to the skirtless model in the long-wave period region and slightly smaller in the short-wave period region.

The potential flow theory model tends to underestimate the drift forces, especially in the long wave period region ($T > 1.3$ s), when it does not account for dissipation ($f = 0$). However, the predictions from the theoretical model improve significantly when considering dissipation within the moonpool, particularly for the wave steepness of $H/\lambda = 0.03$, where the dissipation factor was determined. Despite these improvements, some inconsistencies remain in the short-wave period. Furthermore, the authors found that the additional term in Equation 10 has a minimal effect on the horizontal mean drift forces.

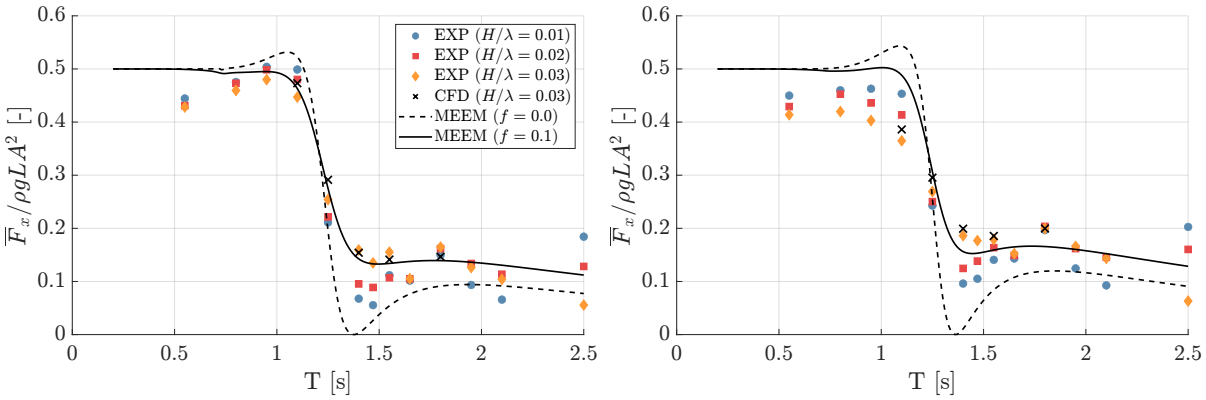

FIGURE 10 – Horizontal mean drift forces using the far-field method in regular waves with various wave steepness : model without (left) and with skirts (right).

VII – Conclusion

We have investigated wave excitation loads on fixed box-like pontoons with a moonpool, equipped with and without skirts. The experiment was carried out in the two-dimensional wave flume of Ecole Centrale Marseille, using regular waves of varying steepness to examine nonlinearity. Dedicated numerical simulations were performed corresponding to the experimental setup to compute the wave excitation forces and free surface elevation around the model as well as the moonpool. The theoretical model was developed for this specific geometry based on the fairly perfect fluid assumption utilizing the two-dimensional matched eigenfunction expansion method.

The study found that the presence of skirts distinctly influences wave excitation forces, both in experiments and numerical simulations. By incorporating dissipation into the moonpool, the potential flow theory model successfully captures the first harmonic wave forces as well as the mean drift forces using the far-field method. In future studies, we plan to broaden our findings to include a freely floating body to investigate how the skirts affect motion responses.

Références

[1] T. Choisnet, B. Geschier, and G. Vetrano. Initial comparison of concrete and steel hulls in the case of ideol's square ring floating substructure. *15th World Wind Energy Conference and Exhibition*, 2016.

[2] T. Choisnet. Annular buoyant body, US9120542B2, 2015.

[3] K. P. Thiagarajan, I. Datta, A. Z. Ran, L. Tao, and J. E. Halkyard. Influence of heave plate geometry on the heave response of classic spars. *International Conference on Offshore Mechanics and Arctic Engineering*, 2002.

[4] B. Molin. On the piston and sloshing modes in moonpools. *Journal of Fluid Mechanics*, 2001.

[5] O. M. Faltinsen, O. F. Rognebakke, and A. R N. Timokha. Two-dimensional resonant piston-like sloshing in a moonpool. *Journal of Fluid Mechanics*, 2007.

[6] A. G. Fredriksen, T. Kristiansen, and O. M. Faltinsen. Wave-induced response of a floating two-dimensional body with a moonpool. *Philosophical Transactions of the Royal Society A : Mathematical, Physical and Engineering Sciences*, 2015.

[7] S.H. Yang, S.B. Lee, J.H. Park, S.Y. Han, Y.M Choi, J. Do, S.H. Kwon, and B. Molin. Experimental study on piston- and sloshing- mode moonpool resonances. *Journal of Marine Science and Technology*, 2016.

[8] S. Ravinthrakumar, T. Kristiansen, B. Molin, and B. Ommani. A two-dimensional numerical and experimental study of piston and sloshing resonance in moonpools with recess. *Journal of Fluid Mechanics*, 2019.

[9] X.B. Chen and S. Malenica. Interaction hydrodynamique d'un ensemble de flotteurs sur la surface libre - une nouvelle méthode de singularies -. *10 emes JOURNÉES DE L'HYDRODYNAMIQUE*, 2005.

[10] P. Gével. Le probléme de diffraction-radiation-premiére partie : Théorémes fondamentaux. *ENSM, Univ. Nantes*, 1982.

[11] F Borisade, T Choisnet, and P W Cheng. Design study and full scale mbs-cfd simulation of the ideol floating offshore wind turbine foundation. *Journal of Physics : Conference Series*, 2016.

[12] A. Courbois, E. Tcheuko, B. Bouscasse, Y.M. Choi, O. Kimmoun, and R. Mariani. Study of viscous effects on wave drift forces on a rectangular pontoon with a damping plate by using cfd code openfoam. *International Conference on Ocean, Offshore and Arctic Engineering*, 2018.

[13] Y. J. Kim. Numerical improvement and validation of a naval hydrodynamics cfd solver in view of performing fast and accurate simulation of complex ship-wave interaction, PhD thesis, 2022.

[14] T. Descamps. Numerical analysis and development of accurate models in a cfd solver dedicated to naval applications with waves, PhD thesis, 2023.

[15] Y.M. Choi, Y. J. Kim, B. Bouscasse, S. Seng, L. Gentaz, and P. Ferrant. Performance of different techniques of generation and absorption of free-surface waves in computational fluid dynamics. *Ocean Engineering*, 2020.

[16] F. J. Mendez and I. J. Losada. A perturbation method to solve dispersion equations for water waves over dissipative media. *Coastal Engineering*, 2004.

[17] C. J. R. Garrett. Wave forces on a circular dock. *Journal of Fluid Mechanics*, 1971.

[18] H. Maruo. The drift of a body floating on waves. *Journal of Ship Research*, 1960.

[19] J. N. Newman. The drift force and moment on ships in waves. *Journal of Ship Research*, 1967.

[20] B. Molin. *Offshore Structure Hydrodynamics*. Cambridge University Press, 1 2023.